Articles

Solution Structure and Backbone Dynamics of the Photoactive Yellow Protein[†,‡]

Petra Düx,[§] Gilles Rubinstenn,[§] Geerten W. Vuister,[§,||] Rolf Boelens,[§] Frans A. A. Mulder,[§] Karl Hård,[§,⊥] Wouter D. Hoff,[#,▽] Arthur R. Kroon,[#] Wim Crielaard,[#] Klaas J. Hellingwerf,[#] and Robert Kaptein*[,§]

Department of NMR Spectroscopy, Bijvoet Center for Biomolecular Research, Utrecht University, Padualaan 8, 3584 CH Utrecht, The Netherlands and Department of Microbiology, E. C. Slater Insitut, BioCentrum Amsterdam, University of Amsterdam, Nieuwe Achtergracht 127, 1018 WS Amsterdam, The Netherlands

Received March 23, 1998; Revised Manuscript Received June 30, 1998

ABSTRACT: The solution structure of photoactive yellow protein (PYP), a photosensory protein from *Ectothiorhodospira halophila*, has been determined by multidimensional NMR spectroscopy. The structure consists of an open, twisted, 6-stranded, antiparallel β-sheet, which is flanked by four α-helices on both sides. The final set of 26 selected structures is well-defined for the regions spanning residues Phe^{6}−Ala^{16}, Asp^{24}−Ala^{112}, and Tyr^{118}−Val^{125} and displays a root-mean-square deviation, versus the average, of 0.45 Å for the backbone and 0.88 Å for all heavy atoms. Comparison of the solution structure with an earlier published 1.4 Å crystal structure (Borgstahl, G. E. O., Williams, D. R., and Getzoff, E. D. (1995) *Biochemistry 34,* 6278−6287) reveals a similarity with a root-mean-square deviation of 1.77 Å for the backbone for the well-defined regions. The most distinct difference in the backbone with the crystal structure is found near the N-terminus, for residues Asp^{19}−Leu^{23}, which corresponds to an α-helix in the crystal structure and to one of the poorest defined regions in the solution structure. To characterize the dynamic behavior of PYP in solution, we undertook a ^{15}N relaxation study and measurements of hydrogen/deuterium exchange. Determination of order parameters through the model-free Lipari-Szabo approach enabled the identification of several regions of enhanced dynamics. The comparison of atomic displacements in the backbone traces of the ensemble structures, with mobility measurements from NMR, show that the poorly defined regions feature fast internal motions in the nanosecond to picosecond time scale.

Photoactive yellow protein (PYP)[1] from *Ectothiorhodospira halophila* is the prototype member of a new family of yellow colored photoreceptors (*1*, *2*), referred to as the xanthopsins (*3*). PYP is water-soluble and shows an absorption maximum at 446 nm with a relatively high extinction coefficient of 45.5 mM^{-1} cm^{-1} (*2*). Video analysis of free-swimming bacteria revealed that the absorption spectrum of PYP matches the wavelength dependence of the negative phototactic behavior of *E. halophila*. Hence, it was suggested that PYP acts as the photoreceptor for negative phototaxis (*4*). In response to illumination, the absorption spectrum of PYP changes in a cyclic fashion. This photocycle involves two intermediates, which are characterized by a red-shifted and a blue-shifted absorption maximum, respectively (*2*, *5*, *6*). The photocycle involves a trans-cis isomerization of the chromophore (*7*, *8*), which was found to be thiol ester-linked *p*-coumaric acid (*9*, *10*). PYP is the best characterized eubacterial photoreceptor and the first example of a protein containing *p*-coumaric acid as a covalently bound cofactor, which has previously only been described as a metabolite in higher plants.

The crystal structure at 1.4 Å resolution of PYP shows a central, 6-stranded, antiparallel β-sheet flanked by five α-helices in an α/β fold (*11*). The hydroxyl group of the chromophore is deprotonated and participates in a hydrogen-bonding network with side chains of surrounding residues, which is also in agreement with results from resonance

[†] This work was supported by The Netherlands Foundation for Chemical Research (SON) and The Netherlands Foundation for Life Science, with financial assistance from The Netherlands Organization for Scientific Research (NWO). G.R. has been financially supported by Rhone-Poulenc (F), G.W.V. by the Royal Netherlands Academy of Arts and Sciences (KNAW), and W.D.H. by the Cancer Research Fund of the Damon Runyon-Walter Winchell Foundation, DRG-1360.

* Corresponding author. E-mail: kaptein@nmr.chem.ruu.nl).

[‡] Atomic coordinates for the 26 final structures have been deposited in the Brookhaven Protein Data Bank, Accession Number 3phy.

[§] Utrecht University.

[||] Present address: Department of Biophysical Chemistry, University of Nijmegen, Toernooiveld 1, 6525 ED Nijmegen, The Netherlands.

[⊥] Present address: ASTRA, Structural Chemistry Laboratory, 43183 Mölndal, Sweden.

[#] University of Amsterdam.

[▽] Present address: Department of Physics, Oklahoma State University, 145 Physical Sciences II, Stillwater, OK 74078-3072.

[1] Abbreviations: PYP, photoactive yellow protein; NMR, nuclear magnetic resonance; ROESY, rotating-frame overhauser enhancement spectroscopy; COSY, correlation spectroscopy; TOCSY, total correlation spectroscopy; DQF, double quantum filtered; TQF, triple quantum filtered, NOESY, nuclear overhauser enhancement spectroscopy; HSQC, heteronuclear single quantum coherence spectroscopy; HMQC, heteronuclear multiple quantum coherence spectroscopy.

S0006-2960(98)00665-5 CCC: $15.00
Published on Web 08/26/1998

Raman spectroscopy (*12*). Time-resolved X-ray diffraction of an intermediate that accumulates with steady-state illumination shows the disruption of this hydrogen-bonding network and a conformational change of the chromophore pocket (*13*).

Considering that PYP is water-soluble at millimolar concentrations and, with its 125 residues, relatively small in size, it presents a unique model system to study photobiological reactions in solution, as is possible with high-resolution NMR techniques. The structural characterization of the ground state of PYP is a first step in this study.

The solution structure of PYP, reported here, consists of a rigid and structurally well defined α/β fold and mobile, solvent-accessible, structurally poorer defined loop regions. The rigid core consists of an open, twisted, 6-stranded, antiparallel β-sheet, enclosed by a sheet-spanning turn and four helices. This three-dimensional fold is similar to the crystal structure (*11*), with local differences in the backbone and some side chain conformations for the well-defined parts of the solution structure. The major difference in the backbone is that no regular secondary structural element is found for the loop region, spanning residues Asp^{19}−Leu^{23}, which is found in an α-helical conformation in the crystal structure. Our study of the structure of PYP in solution is complemented with the measurement of amide exchange rates and analysis of the backbone dynamics using ^{15}N relaxation studies. The resulting data confirm that the internal core of PYP is rather rigid and inaccessible to the solvent, which fits well with the globular scaffold of the molecule. Amide exchange measurements, on the other hand, showed that the 26 N-terminal residues are highly accessible to the solvent. The fact that the solution structure is poorly defined in the loop regions, spanning residues Met^{1}−Ala^{5}, Lys^{17}−Leu^{23}, and Leu^{113}−Ser^{117}, was shown by the relaxation measurements to result from higher backbone mobility. Furthermore, the N-terminal half of α-helix 4 (residues Asp^{53}−Gln^{56}) seems to be more mobile when compared to the other helices.

MATERIALS AND METHODS

Samples. Unlabeled PYP samples were isolated by a modification of Meyer's method (*1*) as described by Hoff et al. (*14*). Isotopically enriched samples were obtained by heterologous overexpression of a polyhistidine-tagged derivative of apoPYP from *E. halophila* in *Escherichia coli*, followed by its in vitro reconstitution with the anhydro derivative of the chromophore as reported by Kort et al. (*3*). Cleavage of histidine-tagged apoPYP was performed at 37 °C for 5−24 h using an enterokinase/PYP ratio of 1:50 (w/w). For preparing uniformly labeled ^{15}N samples, cells were grown on Evans minimal medium (*15*) with 30 mM $^{15}NH_4Cl$ as the sole nitrogen source. For the preparation of a 10% ^{13}C-labeled sample, cells were also grown on Evans minimal medium, but containing 5 g/L glucose of which 10% was labeled with ^{13}C. The extent of labeling of PYP with ^{13}C and ^{15}N was confirmed with electrospray mass spectrometry (data not shown).

The unlabeled and uniformly ^{15}N-labeled PYP samples were solutions of 4 and 2.8 mM, respectively, both in 95%/5% v/v H_2O/D_2O, at pH 5.8, containing 5 mM Tris-HCl. The 10% ^{13}C-labeled sample had a concentration of 2.5 mM, also containing 2.5 mM KH_2PO_4. For the proton/deuterium exchange experiments, a 2.5 mM solution of PYP plus 5 mM Tris-HCl at pH 5.8, in H_2O was freeze-dried and dissolved in D_2O, and the pH was adjusted at 5.8 using DCl and NaOD.

NMR Spectroscopy. Spectra were recorded at 311 K, using either a Bruker AMX 600, a Varian UnityPlus 500, or a Varian UnityPlus 750 spectrometer. 2D ROESY spectra (*16*) were acquired at 298 K, using a 50 ms spin lock consisting of 30° flip angle pulses (*17*) and at 280 K using a frequency-modulated, continuous spin lock of 20 ms duration to study the slow chromophore ring flipping and the ROE interactions involving the hydroxyl protons, respectively. (^{15}N, ^{1}H)-HSQC (*18*), 3D (^{15}N, ^{1}H)-NOESY−HSQC (*19*), 3D (^{15}N, ^{1}H)-TOCSY−HSQC (*19*), and 3D (^{15}N, ^{1}H)-HMQC−NOESY−HSQC (*20*) spectra were recorded, employing gradient coherence selection in conjunction with a sensitivity enhancement scheme (*21*−*23*). The 3D HNHA (*24*), the modified 3D HNHB (*25*), and the ^{15}N-filtered 2D ^{1}H TOCSY (*26*) spectra were acquired as described before. Processing of the data was carried out using the in-house written software package TRITON. For analysis the REGINE software package (*27*) was used. Proton chemical shifts are referenced relative to the water resonance at 4.65 ppm (311 K) and ^{15}N relative to ammonium chloride at 22.3 ppm. Carbon chemical shifts, obtained from the natural-abundance gradient-enhanced ^{13}C−HSQC (*28*), are relative to the glucose $^{13}C_\alpha$, taken as 76.536 ppm.

Relaxation and Exchange Measurements. All measurements were recorded at 311 K on the 2.8 mM ^{15}N-labeled sample. Heteronuclear NOE spectra and ^{15}N T_1 and ^{15}N $T_{1\rho}$ relaxation experiments were recorded as described earlier (*29*−*31*) using pulsed-field gradients for coherence selection in combination with a sensitivity enhancement scheme (*21*−*23*). The longitudinal ^{15}N relaxation rates $R(N_z)$ were determined from a series of twelve spectra with delays of 100, 200, 300 (2×), 400, 500, 600 (2×), 700, 800, 1000, and 1200 ms. The transverse in-phase ^{15}N relaxation rates (*32*), $R(N_{\rho z})$, were determined from a series of twelve spectra with delays of 14, 30 (2×), 40, 50, 60, 70, 90, 110, 150 (2×), and 200 ms, using a nitrogen spin lock with a 2.3 kHz field strength. The heteronuclear cross relaxation rates $R(H_z \rightarrow N_z)$ were derived from two series of spectra, recorded with and without 3.5 s of proton saturation of the amide protons, respectively. The proton/deuterium exchange rates were obtained from a series of 28 ^{15}N HSQC spectra, recorded from 20 min to 51 h after dissolving the freeze-dried sample in D_2O. Each (^{15}N, ^{1}H)-HSQC experiment was recorded in 9 min. All data were processed on Silicon Graphics Indy workstations using the software package NMRPipe (*33*).

The relaxation data were analyzed using in-house developed software (*31*). The longitudinal ^{15}N relaxation rates, $R(N_z)$, and the transverse in-phase ^{15}N relaxation rates, $R(N_{\rho z})$, as well as the proton/deuterium exchange rates, were obtained by curve fitting of a two-parameter monoexponential function through the peak intensities, using the Levenburg−Marquardt algorithm (*34*). The uncertainties in the peak intensities were set equal to the average thermal noise level of the spectra. The rmsd values between the calculated and the experimental intensities were used to assess the uncertainties in the relaxation parameter in a Monte Carlo

analysis with 500 simulated data sets. $R(H_z \rightarrow N_z)$ were calculated from the NOE enhancement $\eta = (\gamma_H/\gamma_N)R_N(H_z \rightarrow N_z)/R_N(N_z)$ where γ_H and γ_N are the gyromagnetic ratios of ^{1}H and ^{15}N nuclei, respectively. Uncertainties in $R(H_z \rightarrow N_z)$ were obtained using standard error propagation.

Structure Calculations. NOE intensities assigned to distances in unambiguously identified secondary structure elements, such as $d_{\alpha N}(i, i + 3)$ for α-helices and $d_{\alpha N}(i, j)$ for *β*-sheets, were used to calibrate the NOE intensities. Successively they were classified as strong, medium, or weak, and thereby placed into categories with upper bounds set to 2.6, 3.6, and 4.5 Å for the 2D NOE and 2.8, 3.6, and 5.0 Å for the heteronuclear NOESY-derived distances. Lower bounds were set to the sum of the van der Waals radii (1.8 Å). Distances originating from overlapping peaks in the NOESY were set to 4.5 Å. Twelve constraints were derived from 3D (^{15}N,^{1}H)-HMQC−NOESY−HSQC. Nine constraints involving hydroxyl protons were obtained from a NOESY at 288 K with a mixing time of 100 ms using a WATERGATE detection scheme. Fifty-eight ϕ, seven ψ, four χ_1, five χ_2, and one χ_3 dihedral constraints were extracted from the analysis of 3D HNHA and 3D HNHB spectra. Stereospecific assignments for seven glycines were derived as described before (*25*).

From measurements of the proton/deuterium exchange rates (see below), 31 slowly exchanging amide protons were identified. These were located in regular secondary structure elements involved in hydrogen bonding and translated into distance constraints between the respective amide proton and the appropriate oxygen, as well as between the corresponding nitrogen and oxygen atoms.

Structures were generated by using distance geometry (DG), followed by a simulated annealing regularization (DGSA), and a simulated annealing refinement as implemented in X-PLOR 3.1 (*35*−*37*). A new residue in the X-PLOR topology file was defined for the *p*-coumarate chromophore, covalently linked to the Cys^{69}. On the basis of the results from X-ray crystallography (*11*) and resonance Raman spectroscopy (*12*), the chromophore was considered to be deprotonated. The regularization step of the embedded structures consisted of a 12 ps molecular dynamics simulation at 2000 K, followed by a cooling part of 0.16 ps and two successive constrained refinement steps of 0.47 and 0.58 ps, respectively, with an initial temperature of 2000 K, excluding electrostatic interactions.

Selection and Analysis. Twenty-six out of forty calculated structures were selected on the basis of low total energy. All subsequent numerical analysis was performed using X-PLOR 3.1 (*37*), INSIGHT II (Biosym/MSI), PROCHECK−NMR (*38*), PROMOTIF (*39*), or in-house written software. For the preparation of the figures, structures were visualized with the programs MOLMOL (*40*) and INSIGHT II (Biosym/MSI).

RESULTS

NMR Assignments. Spin system and sequential assignments of PYP were obtained according to standard methods applicable to unlabeled samples (*41*), with the support of 3D (^{15}N, ^{1}H)-TOCSY−HSQC, 3D (^{15}N, ^{1}H)-NOESY−HSQC, DQF− and TQF−COSY (*42*, *43*), clean-TOCSY (*44*), NOESY (*45*), and 3D TOCSY−NOESY spectra (*46*, *47*). In addition, a 2D gradient-enhanced, natural-abundance (^{13}C, ^{1}H)-HSQC was used (*28*) to distinguish geminal from vicinal protons. This yielded assignments for 90% of the protons in PYP (cf. supplementary Table 1). For Met^1 and Glu^2 no resonances were found at all, whereas for His^3 only backbone resonances could be identified. As neither the amide nor the H_α resonances of His^3 show any NOEs to other residues, the N-terminus is most probably unstructured. Stereospecific assignment of the diastereotopic methyl groups of valine and leucine residues was performed using a 10% ^{13}C-enriched sample (*48*).

The vinyl protons of the chromophore could be identified in the aromatic region in TOCSY and COSY spectra by their characteristic 16 Hz doublet splitting, which is in accordance with a trans conformation. The remaining signals of the chromophore ring were assigned by combination of TOCSY, COSY, and ROESY data. All assignments are listed in supplementary Table 1 and will be submitted to the BioMagResBank.

Overall Structural Fold and Structure Quality. Figure 1B shows the backbone traces of the ensemble of 26 selected structures. The calculations were based on 1352 distance and 75 dihedral constraints, as described in the Experimental Section and shown in Figure 2A. The ensemble of 26 structures has a total of six dihedral constraint violations above 5°, with a maximum violation of 8.0°, and two distance constraint violations above 0.5 Å (0.52 and 0.63 Å). A stereoview of a ribbon representation of the refined average

Table 1: NMR Structure Statistics for PYP

A. Structural Statistics for the Final 26 Structures

rmsd from experimental distance constraints (Å)	
all (1351)	0.054 ± 0.001
intraresidual (315)	0.050 ± 0.002
sequential ($\|i - j\| = 1$) (344)	0.044 ± 0.005
medium range ($1 < \|i - j\| < 5$) (230)	0.059 ± 0.004
long range ($\|i - j\| \geq 5$) (431)	0.064 ± 0.004
H-bond (31)[a]	0.047 ± 0.009
number of distance constraint violations >0.5 Å[b]	2 (0.52 Å, 0.63 Å)
rmsd from experimental dihedral constraints (deg) (75)[c]	0.064 ± 0.019
number of dihedral constraint violations >5°[d]	6 (max 8°)
deviations from idealized covalent geometry:	
bonds (Å)	0.004 ± 0.000
angles (deg)	0.704 ± 0.011
impropers (deg)[e]	0.556 ± 0.025
Lennard-Jones van der Waals energy (kcal mol^{-1})[f]	−112 ± 27

B. Atomic rms Differences (Å) Versus Average Structure

	backbone	all heavy atoms
residues 6−16, 24−112, 118−125	0.45 ± 0.07	0.88 ± 0.06
residues 4−125	0.84 ± 0.20	1.24 ± 0.17

[a] For each hydrogen bond, two distance constraints were used: $r_{NH-O'}$, 1.7−2.5 Å; and $r_{N-O'}$, 2.3−3.5 Å. [b] Constraint violations > 0.5 Å are listed between brackets. [c] The torsion angle constraints comprise fifty eight ϕ, seven ψ, four χ_1, five χ_2, and one χ_3 angles. The minimum ranges employed for these constraints were ±10°, ±5°, ±40°, ±40°, and ±120°, respectively. [d] Maximum violation is listed between brackets. [e] The improper torsion constraints serve to maintain planarity and chirality. [f] Calculated with CHARMM (49) empirical energy function. Note that this term is not included in the target function used for simulated annealing and restrained minimization.

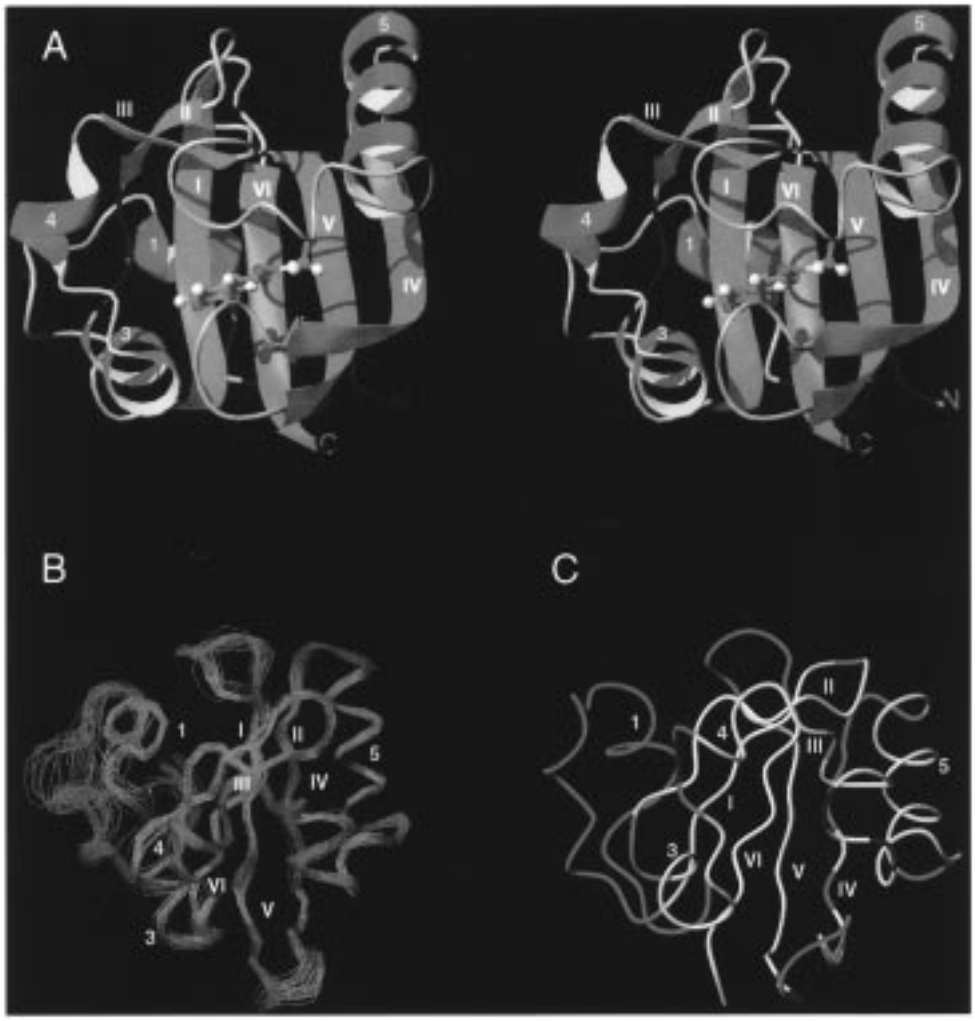

FIGURE 1: Representations of the NMR solution structure of PYP. The β-strands are labeled by latin and the α-helices by arabic numbers, in accordance with the numbering in the crystal structure. (A) Stereoview of the ribbon presentation of the refined average structure, prepared using MOLMOL (*40*). The chromophore is displayed by balls and sticks (green carbons, white hydrogens, red oxygen, and one yellow sulfur). The β-sheet is in blue (including β-strands I−VI), the α-helices in red/yellow (including α-helices 1−5), and all loops and turns in gray. (B) Backbone traces of the ensemble of 26 NMR-derived structures, superimposed on all atoms spanning residues Val^{4}−Val^{125}. The traces have been color coded according to S^2, derived from a two-parameter Lipari-Szabo approach, ranging from blue (small motion amplitude, larger S^2) to red (larger motion amplitude, smaller S^2). S^2 values of residues for which no relaxation parameters could be extracted were derived from interpolation. (C) Mapping of the proton/deuterium exchange rates onto the minimized average NMR structure. The backbone trace is color coded according to the exchange rate of the backbone amide protons, as red, yellow, and white for class I (fast), class II (interm.), and class III (slow), respectively. Prolines are colored blue.

structure is shown in Figure 1A. The protein has an α/β type fold consisting of an open, twisted, 6-stranded, antiparallel β-sheet, flanked by four α-helices and a long, well-defined loop containing Cys^{69}, which is linked to the chromophore. The core of the protein is very well defined, as is displayed by the local rmsd values for the backbone of the polypeptide chain (cf. Figure 2C). Three regions of larger structural variability can be identified, spanning residues Met^{1}−Ala^{5}, Lys^{17}−Leu^{23}, and Leu^{113}−Ser^{117}. As will be shown below, the disorder in these latter regions coincides with increased mobility of the polypeptide backbone. Excluding these parts, the ensemble of structures has an rmsd versus the average of 0.45 ± 0.07 Å for the backbone and 0.88 ± 0.06 Å regarding all heavy atoms (cf. Table 1).

The Ramachandran plot for the well-defined part of the protein (supplementary Figure 1) shows that 72.1% of the nonglycine and nonproline residues are found in the most favored region, 23.0% in the additionally allowed regions, and 2.9% in the generously allowed regions; 2% of the nonglycine and nonproline residues fall in the disallowed region. Among these outliers are Asn^{43} (see below) and Asp^{53} in four structures of the ensemble, which are the first residues of the second and third α-helices in the solution structure, respectively. A summary of all structural statistics is given in Table 1.

The secondary structure elements were analyzed using the program PROMOTIF (*39*) by means of the DSSP routine (*50*) and by mapping medium- and long-range NOE patterns and $^{3}J_{HNH\alpha}$ coupling constraints typical for helices and β-sheets (*41*). In the following, the numbering of the helices of the solution structure corresponds to the one of the crystal structure for a more convenient comparison. Helix 1, spanning residues Asp^{10}−Leu^{15}, is located in the well-defined part of the N-terminal region. It is followed by a poorly defined loop region, residues Lys^{17}−Leu^{23} and the first β-hairpin. The first two β-strands are made up of Ala^{27}−Asp^{34} and Asn^{38}−Leu^{40} and are connected by a tight turn.

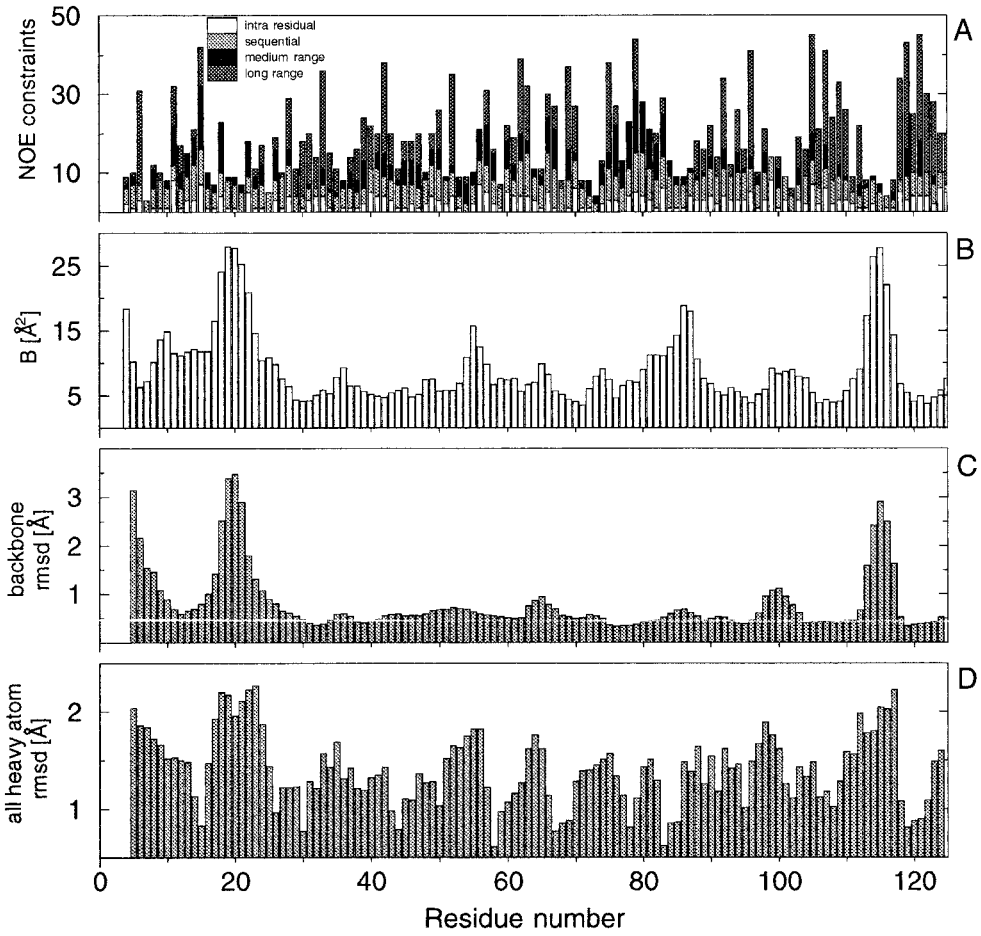

FIGURE 2: Overview of structural parameters of PYP versus residue number. (A) Number of distance constraints per residue. The constraints are classified as long-range, medium-range, sequential, and intraresidual as defined in Table 1. (B) Average crystallographic temperature factors (*B* value) for the backbone C_α, N, and C′ atoms (PDB accession code: 2phy). (C) Pairwise rmsd for the backbone C_α, N, and C′ atoms in the ensemble of NMR structures. (D) Pairwise rmsd for all heavy atoms.

A bulge is formed in this β-hairpin, comprising residues Asp[34], Gly[37], and Asn[38], as well as Gln[32], Leu[40], and Gln[41] and pointing across the β-sheet toward α-helix 5. Two short α-helices flank the outside of the second strand, α-helix 3 (residues Asn[43]−Thr[50]) and α-helix 4 (residues Asp[53]−Ile[58]). The third β-strand, comprising Lys[60], Asn[61], and Phe[62], is followed by a long, well-defined loop containing Cys[69], which is linked to the chromophore. This loop crosses the whole β-sheet on its front side, as shown in the orientation of the protein in Figure 1A. On the right-hand side of the sheet it leads into α-helix 5, which starts at Phe[75] and ends with Gly[86]. This relatively long helix flanks the outside of β-strand IV, which comprises the residues Leu[88]−Phe[96]. β-strand IV is connected with strand V by a rather well-defined loop, which bends toward the chromophore. The β-strand V spans residues Thr[103]−Lys[111] and leads via the previously mentioned, poorly defined loop into strand VI, comprising residues Trp[119]−Val[125]. The C-terminal β-strand aligns with the N-terminal strand in the middle of the sheet.

In 38% of the structures a 3_{10}-helix (the hypothetical helix 2) is defined by PROMOTIF for residues Asp[20] to Asp[24] or Gln[22] to Leu[26] in the poorly defined loop region. However, no consistent NOE patterns, indicative of a helix, could be found originating from this region. Furthermore, in 31% of the structures PROMOTIF defines a long turn instead of α-helix 4 (residues Asp[53]−Ile[58]). The medium-range NOEs of these residues are indicative of an α-helix, and the lack of sequential- and long-range NOEs for the N-terminal half of α-helix 4 (cf. Figure 2A) could be the cause for an incomplete α-helix formation. All other α-helices are very well defined in all structures.

The hydrophobic core of PYP consists of residues on both sides of the central β-sheet and is consistent with the crystal structure.

Reduced Spectral Density Function Mapping from Three Relaxation Parameters. Using a recently described procedure for reduced spectral density mapping (*31*, *51*, *52*) the three relaxation parameters ^{15}N T_1, ^{15}N $T_{1\rho}$, and ^{15}N{^{1}H}-NOE (cf. supplementary Table 2) were translated into values for the spectral densities $J_{\mathrm{eff}}(0)$, $J(\omega_{\mathrm{N}})$, and $J_{\mathrm{avg}}(\omega_{\mathrm{H}})$ for 106 out of the 121 backbone nitrogens of PYP. In addition to the four prolines, the first three N-terminal residues, as well as Gly[7] and Glu[12], show no detectable cross-peaks in the (^{15}N, ^{1}H)-HSQC spectra, whereas overlap prevented the analysis for 10 residues (Ser[8], Asp[10], Asn[13], Lys[17], Tyr[42], Lys[60], Lys[64], Phe[96], Thr[103], and Arg[124]). The values for the spectral densities $J(\omega)$ for the backbone ^{15}N-^{1}H vectors of PYP are presented in Figure 3A−C (and in supplementary Table 2). Following the procedure described by Lefèvre et al. (*52*) regression of $J(\omega_{\mathrm{N}})$ versus $J_{\mathrm{eff}}(0)$ for each NH vector of the protein backbone (cf. supplementary Figure 2) yielded an overall rotational correlation time of 6.4 ± 0.6 ns. From τ_{c}, the spectral densities were calculated for a rigid isotropically tumbling macromolecule and these values have been

Table 2: Different χ_1 and χ_2 Dihedral Angles in Solution and Crystal Structure[a]

residue	NMR structure (deg)		crystal structure (deg)	
	A. χ_1 Dihedral Angles			
Ile[31]	78 ± 5	(g^-)	-56	(g^+)
Lys[80]	-100 ± 9	(g^+)	73	(g^-)
Tyr[98]	71 ± 16	(g^-)	182	(t)
Val[107]	-41 ± 18	(g^+)	179	(t)
Trp[119]	52 ± 4	(g^-)	-70	(g^+)
Lys[123]	218 ± 14	(t)	75	(g^-)
	B. χ_2 Dihedral Angles			
Ile[31]	88 ± 5	(g^-)	172	(t)
Leu[33]	176 ± 3	(t)	-55	(g^+)
Tyr[42]	64 ± 7	(g^-)	-81	(g^+)
Lys[78]	-37 ± 1	(g^+)	167	(t)
Phe[79]	-77 ± 2	(g^+)	80	(g^-)
Tyr[118]	-78 ± 3	(g^+)	77	(g^-)

[a] With ideal values for $g^- = (64° \pm 16°)$, $t = (184° \pm 17°)$, and $g^+ = (-67° \pm 15°)$ from Morris (*62*).

indicated as horizontal solid lines in Figure 3A−C. For PYP, all values of $J_{eff}(0)$ are smaller than the rigid-body value, suggesting the absence of millisecond to microsecond time scale motions. Furthermore, the narrow range of $J_{eff}(0)$ and $J(\omega_N)$ values indicates a globular and rather rigid scaffold for the protein. Nevertheless, low values of $J_{eff}(0)$, indicative of internal motions in the nanosecond to picosecond time scale, are found for eight regions, Val[4]−Ala[5], Ala[16]−Leu[23], Gly[35]−Asp[36], Arg[52]−Val[57], Phe[63]−Val[66], Ser[72]−Phe[75], Asn[87]−Leu[88], and Leu[113]−Ser[117], and for a few isolated residues, Glu[46], Glu[93], Thr[95], and Thr[101]. A similar pattern is found for the $J(\omega_N)$ values. Due to a lower precision, the $J_{avg}(\omega_H)$ values only allow identification of three regions with significantly larger values, that it, Val[4]−Ala[5], Met[18]−Gln[22], and Lys[111]−Asp[116].

Model-Free Approach and Order Parameter. Using the model-free approach proposed by Lipari and Szabo (*55*, *56*), the motion of the NH bond vector was also characterized in terms of the overall isotropic tumbling time τ_m, the order parameter S^2, and the internal correlation time τ_e due to fast internal fluctuations:

$$J(\omega) = \frac{2}{5}\left(\frac{S^2\tau_m}{1 + (\omega\tau_m)^2} + \frac{(1 - S^2)\tau_{eff}}{1 + (\omega\tau_{eff})^2}\right)$$

where the effective correlation time $\tau_{eff}^{-1} = \tau_m^{-1} + \tau_e^{-1}$. Following the procedure described by Vis et al. (*31*) we obtained $\tau_m = 6.0 \pm 0.3$ ns, from the average of the 71 most relevant fits ($\chi^2 \leq 1$), which is similar to the result obtained by the reduced spectral density mapping. A subsequent two-parameter fit was satisfactory to determine the order parameters S^2.

As expected from the reduced spectral density mapping results, the order parameter S^2 (Figure 3D) is high on average and shows little variation. The value over the ensemble is 0.85 ± 0.07, which compares very well with values found for well-defined protein cores (*57*−*60*) . Figure 1B depicts the ensemble of 26 NMR structures, where the backbone ribbons are colored according to the value of S^2, ranging from blue (small motional amplitude) to red (large motional amplitude). It is clear that the poorly defined parts, spanning Val[4]−Ala[5], Lys[17]−Leu[23], and Leu[113]−Ser[117], coincide with regions of low S^2 values.

Anisotropic rotational diffusion has not been included in the above analyses. The components of the rotational diffusion tensor **D** were determined from the relaxation data as described by Brüschweiler et al. (*53*) and Lee et al. (*54*). It was found that D_{xx} and D_{yy} differ by only 5% and that ($D_{xx} + D_{yy}$) and D_{zz} differ by only 8% (with a goodness-of-fit χ^2 of 348 (*54*)). This means that, to good approximation, PYP is a spherical rotor and tumbles isotropically.

Proton/Deuterium Exchange Rates. Proton/deuterium exchange rates were measured for the 106 amide protons for which an isolated ^{15}N HSQC cross-peak has been observed. The exchange rates were then grouped into three classes. Class I contains the fast exchanging protons for which no cross-peak can be found in the first HSQC ($T_{1/2} <$ 5 min). Class II contains the protons for which a monoexponential decay can be fit (5 min $< T_{1/2} <$ 60 h). Class III contains the protons that did not show any significant decay of the cross-peak intensity after 50 h ($T_{1/2} >$ 60 h). For the twelve residues with overlapping ^{15}N HSQC cross-peaks, the exchange rates were estimated. The average solvent accessibility values of the backbone, determined on the basis of the ensemble of NMR structures, using the WHATIF program (*61*) with a probe radius of 1.4 Å, are respectively 38, 28, and 9 Å^2 for the residues of class I, II, and III.

Figure 1C depicts the PYP backbone color coded according to the exchange rate. Residues of class I are colored red, residues of class II are colored yellow, and residues of class III are colored white. PYP possesses an internal core, highly inaccessible to the solvent, bordered by regions of variable accessibility. All amides of the inner strands of the β-sheet (I, II, V, VI) belong to class III. The external strand IV shows a characteristic pattern of successive slow and fast exchanging amide protons identifying residues Thr[90], Phe[92], Tyr[94], and Phe[96] being as hydrogen bonded to the residues in the opposite strand V. It is noteworthy that the aromatic side chains of Phe[92], Tyr[94], and Phe[96] cluster in the chromophore core. Helix 5 shows intermediate exchange rates, but residues Tyr[76] and Phe[79], which have their amide protons oriented toward the core, belong to class III. The group of fast exchanging amides includes the poorly defined regions of the ensemble of NMR structures discussed above. These are positioned in the three loops between α-helix 5 and strand IV, between strand IV and V, and between strand V and VI, as well as the entire initial N-terminal part of the protein, up to residue Ala[27], Phe[28], and Gly[29], which show intermediate exchange rates. In addition, the external strand III of the β-sheet belongs to the category of fast exchanging amides.

DISCUSSION

Comparison with Crystal Structure. The fold of the refined average NMR structure and the crystal structure (*11*) of the dark state of PYP correspond very well with a pairwise rmsd of 1.77 Å for the backbone, excluding the poorly defined regions (residues Met[1]−Val[5], Lys[17]−Leu[23], and Leu[113]−Ser[117]). A superposition of C_α tracings of the PYP crystal structure and the PYP NMR structure is shown in Figure 4. A small local difference was found in the β-hairpin, formed by β-strands I and II, where the ψ dihedral angle of Asp[34] is $141° \pm 13°$ in the NMR-derived structure, whereas it adopts a value of $-178°$ in the crystal structure.

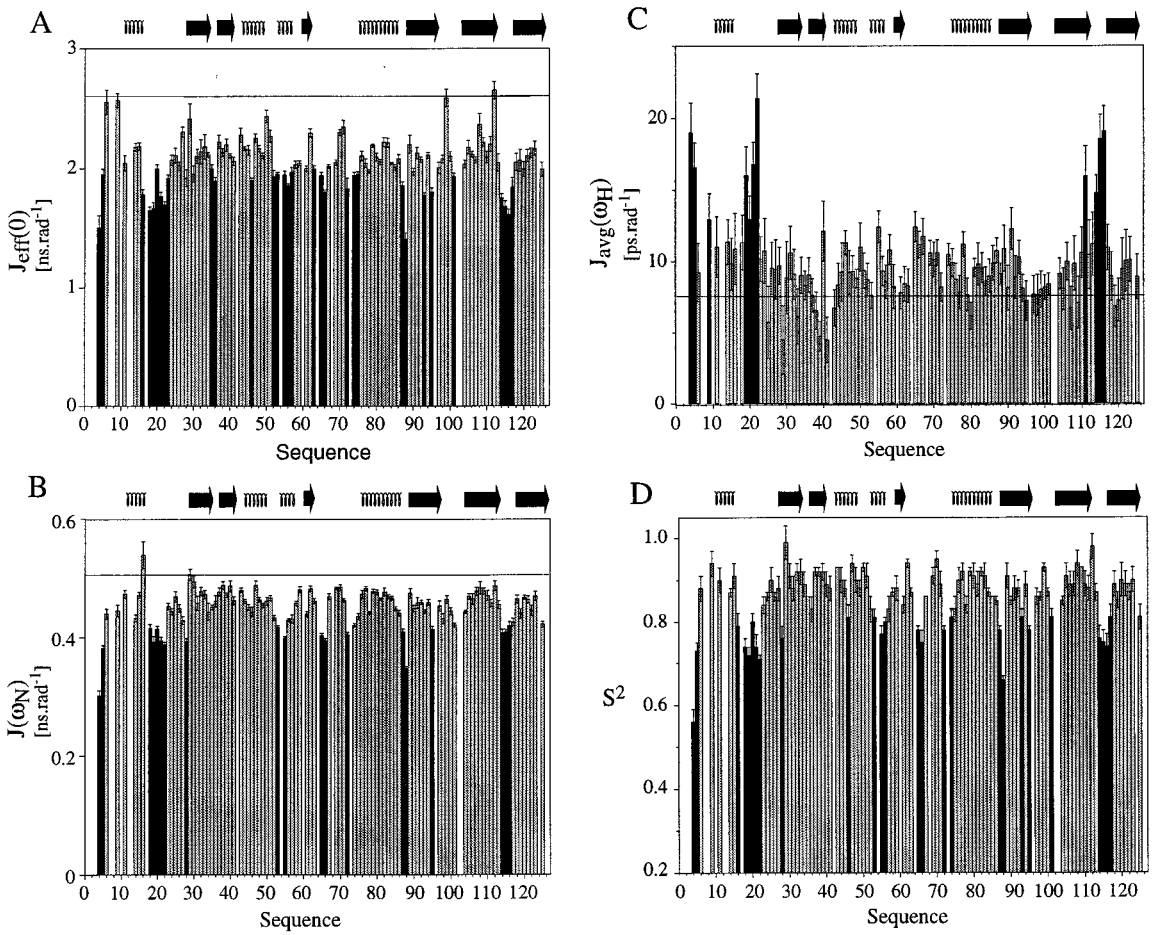

FIGURE 3: Reduced spectral density values and order parameters for the backbone ^{15}N-^{1}H vectors of PYP versus residue number: (A) $J_{eff}(0)$, (B) $J(\omega_N)$, (C) $J_{avg}(\omega_H)$, and (D) order parameter S^2. The secondary structure elements of PYP as determined from the NMR solution structure are depicted on top of each panel. Residues presenting enhanced mobility in the nanosecond to picosecond time scale are highlighted in black. In panels A, B, and C, a continuous line is drawn at the theoretical value for a rigid, isotropically tumbling molecule with a rotational correlation time τ_c of 6.4 ns. Slow internal motions on the millisecond to microsecond time scale would result in positive deviations from the rigid-body value for $J_{eff}(0)$ (panel A). Fast internal motions on the nanosecond to picosecond time scale appear as positive deviations from the rigid-body value for $J_{avg}(\omega_H)$ (panel C) and negative deviations for $J_{eff}(0)$ and $J(\omega_N)$ (panels A and B, respectively).

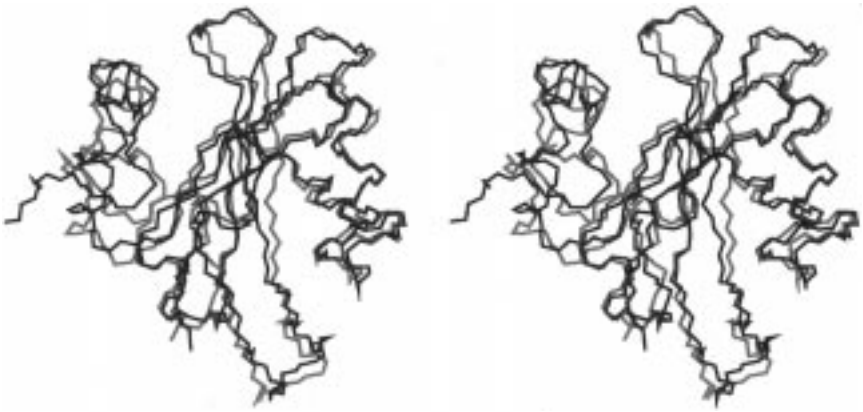

FIGURE 4: Stereoview of the superposition of the NMR structure of PYP (red) and the crystal structure (blue, ref *11*). For the NMR structure the structure from the ensemble closest to the average has been taken. The view is the same as that of Figure 1, parts B and C.

This results in a less pronounced bending of the bulge in this β-hairpin toward α-helix 5. The most obvious differences with the crystal structure are found in the N-terminus. In the crystal structure the N-terminal 28 residues form a lariat-like loop structure, including α−helix 1, α-helix 2, and an N-terminal loop, which bends into the space between α-helix 1 and α-helix 2. In the NMR-derived structure this loop bends toward β-strand VI, so that the main chain hydrogen bonds from residues 2 and 4 to residues 25 and 27, as observed in the crystal structure, are not present. Moreover, residues Asp^{19}−Leu^{23} are found in α-helical conformation in the crystal structure, whereas this region corresponds to one of the poorest defined regions in the NMR-derived structure.

The majority of the side chains, which are well-ordered in the solution structure, have similar conformations in both

the NMR- and X-ray-derived structures. Excluding the 26 residue N-terminal region (in which only Ile[11], Thr[14], and Leu[15] have ordered side chains), as well as residues Leu[113]–Ser[117], the solution and crystal structure superimpose with an rmsd of 1.88 Å for all heavy atoms. Six of the well-ordered side chains show a significantly different conformation when compared to the crystal structure. The χ_1 values of these residues differ considerably and are listed in Table 2A. Another six residues with well-defined side chain positions in the solution structure show significantly different χ_2 values than in the crystal structure and are listed in Table 2B. However, with the exception of Lys[78], the different χ_2 torsion angles do not translate into significantly different positions of the respective side chains. In the crystal structure Lys[78] is located at the surface formed by α-helix 5 and β-strand IV and facing the ring of Phe[92], whereas in the NMR-derived structure it is exposed to the solvent.

The Chromophore Environment. ROESY spectra display a conformational exchange between the δ_1- and the δ_2-protons of this ring, suggesting that the chromophore ring is flipping on a time scale of the ROESY mixing time (50 ms). Yet, the chromophore is tightly packed between the surrounding side chains of residues from α-helix 3 (Glu[46], Thr[50]), as well as the α-helix 3 preceding residue Tyr[42], α-helix 4 preceding residue Arg[52], residue Phe[62] from strand III, from the chromophore-containing turn (Val[66], Ala[67], and Thr[70]), β-strand IV (Tyr[94], Phe[96], Tyr[98]), and by Met[100]. With the exception of Arg[52], Glu[46], and Tyr[98], these residues superimpose within less than 1.2 Å rmsd in the solution and crystal structure.

NOESY spectra, recorded at temperatures below 25 °C, using the WATERGATE technique for supression of the H_2O resonance, show signals at 13.63 and 15.21 ppm, which are identified as originating from hydroxyl protons. Figure 5 depicts the NOE ladders of these hydroxyl protons from a NOESY spectrum recorded at 15 °C. An ROE cross-peak between the OH resonances is also observed in ROESY spectra, recorded at 15 °C, which indicates that the two hydroxyl groups must be positioned in close proximity to each other. From comparisons of these NOE patterns, the signal at 13.63 ppm can be assigned to the hydroxyl proton of Tyr[42], while the signal at 15.21 ppm corresponds to the hydroxyl proton of Thr[50]. The crystal structure shows that the carboxyl group of the side chain of Glu[46] is protonated. From the NOE patterns of the OH resonances it cannot be excluded that this carboxyl proton overlaps with the OH resonances of Tyr[42] or Thr[50]. The crystal structure shows hydrogen bonds between the phenolic oxygen of the chromophore ring with the hydroxyl group of Tyr[42] and the protonated carboxyl of Glu[46]. The hydroxyl of Thr[50] is involved in a hydrogen-bonding network with the hydroxyl oxygen of the Tyr[42] ring and the backbone carboxyl of Glu[46]. The existence of this hydrogen-bonding network is confirmed by the results from the NMR-derived structure.

Strikingly, in the NMR ensemble, the side chain of Arg[52] samples two conformations: in the larger part of the ensemble it clusters above the chromophore ring (cf. Figure 6A), whereas in a smaller part its guanidinium group is positioned above the aromatic ring of Tyr[98] (cf. Figure 6B). In neither conformation does Arg52 hydrogen bond with the carbonyl oxygen atoms of Thr[50] and Tyr[98], as it does in the crystal structure. In the solution structure the aromatic ring

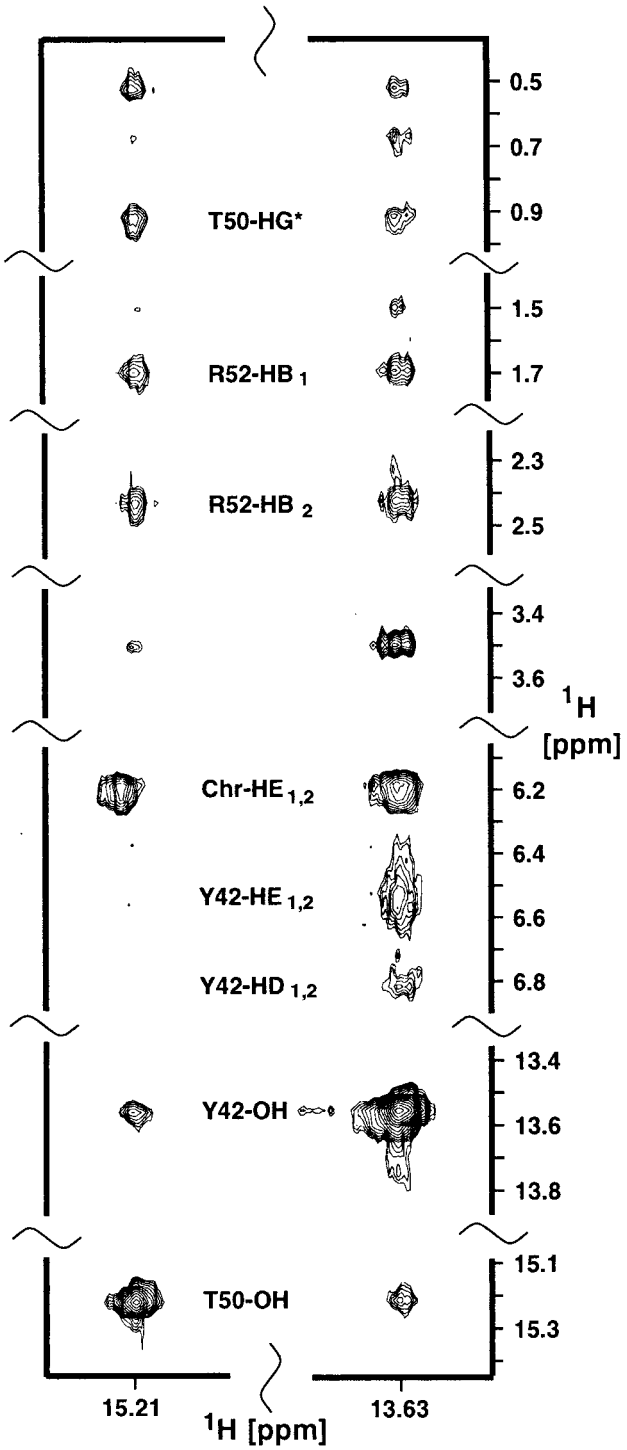

FIGURE 5: Section of the 2D NOESY spectrum at 15 °C depicting NOEs of the two hydroxyl resonances, which were assigned to the hydroxyl protons of Tyr[42] and Thr[50]. Selected NOEs have been labeled.

of Tyr[98] is facing the loop between α-helix 3 and 4, sideways to the chromophore, while in the crystal structure the side chain of Tyr[98] is oriented toward the chromophore-containing loop (cf. Figure 6C). Scrutton and Raine (*63*) recently reviewed the evidence that positively charged amino groups tend to pack between 3.4 and 6 Å of the centroids of aromatic rings. Such amino-aromatic interactions have been recognized as important associations that contribute to the stability of the protein's architecture. In the solution structure of PYP in one part of the ensemble the $N^{\eta 1}$ and $N^{\eta 2}$ amino groups

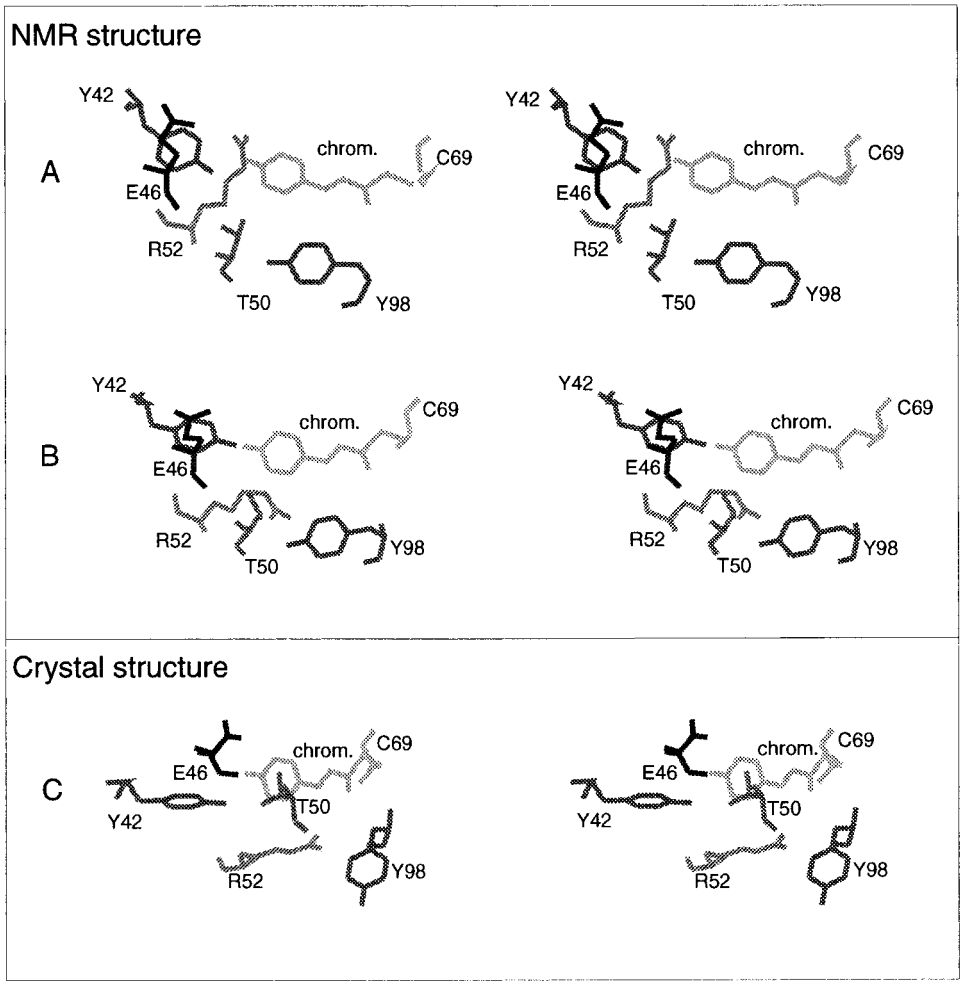

FIGURE 6: Stereoviews of the region of PYP around the chromophore. The two subclasses A and B of the NMR structures differ predominantly in the conformations of Arg^{52} . C is the crystal structure.

of Arg^{52} pack within 4.2 ± 0.7 and 3.8 ± 0.7 Å, respectively, of the chromophore ring and within 8.0 ± 1.0 and 8.2 ± 0.7 Å of the ring of Tyr^{98}. In another cluster $N^{\eta 1}$ and $N^{\eta 2}$ are located whithin 6.5 ± 0.4 and 6.1 ± 0.7 Å, respectively, of the chromphore ring and within 4.4 ± 0.6 and 4.0 ± 0.9 Å of the ring of Tyr^{98}. It seems that the amino groups of Arg^{52} preferentially take a position within 4 Å of the nearby aromatic rings, thus contributing to the overall stability of PYP. In contrast, in the crystal structure, the different position of the Tyr^{98}-ring prevents an interation of the amino groups of Arg^{52} with this ring (cf. Figure 6C). Furthermore, the guanidinium group is flanking the chromophore ring sideways (within 6.3 and 7.1 Å, respectively for $N^{\eta 1}$ and $N^{\eta 2}$, from its centroid, i.e., beyond stabilization distance (*63*)) shielding the chromophore from solvent (Figure 6C). Genick and co-authers (*64*) have recently concluded, on the basis of site-directed mutagenesis studies, that Arg^{52} is not required for charge stabilization of the chromophore. This fits with our observation that in a significant number of PYP structures Arg^{52} interacts with Tyr^{98}, rather than with the chromophore.

NMR-Detected Mobility. Disorder in the NMR-derived structure originates from a lack of structural constraints, which may or may not be due to local mobility. The results from ^{15}N relaxation measurements show that residues in the three poorly defined regions (Met^1−Ala^5, Lys^{17}−Leu^{23}, Leu^{113}−Ser^{117}) have significantly lower S^2 values. This indicates that the structural heterogeneity is brought about by fast internal motions. Also, the crystallographic *B* factors, which are related to the mean-square fluctuations of the atoms from their average position, are significantly higher for these regions (compare Figure 2B with Figure 3D). It is noteworthy that the residues Asp^{19}−Leu^{23}, which are ill-defined in the NMR ensemble, are found in an α-helical conformation in the crystal structure (α-helix 2). In a recent molecular dynamics study van Aalten (personal communication) found that this helix is involved in concerted motions with the loop spanning residues Thr^{50}−Asp^{53} and α-helix 1. The difference between the NMR and X-ray structure in this region may be due either to the crystalline environment or to differences in experimental conditions. Higher local rmsd values and *B* factors are also observed for Asp^{65} and Val^{66}, which are corroborated by lower S^2 values. Thus, also the N-terminal part of the chromophore loop exhibits motions in the nanosecond to picosecond time scale. Residues Tyr^{98}, Gln^{99}, Met^{100}, and Thr^{101} show higher rmsd values, which is reflected in the higher mobility of Met^{100}. The latter is located close to the chromophore, where also Glu^{46} and Tyr^{94} are displaying higher mobility.

Finally, the N-terminal half of α-helix 4 (residues Asp^{53}−Gln^{56}) seems to be less rigid when compared to the other helices. This is also reflected in the incomplete definition of this α-helical conformation in all structures of the NMR ensemble. It is noteworthy that α-helix 4 belongs to a structurally conserved region (*65*), which PYP shares with

several other proteins involved in signaling and circadian rhythmicity, called the PAS domain (termed after the first described PAS domain proteins: *per*, *arnt*, and *sim* (*66*)). PAS is 37% homologous with PYP in the region of residues Gly^{21}−Lys^{66}, comprising part of the highly mobile N-terminal region, β-strand I, II, and III, as well as α-helices 3 and 4, and the N-terminal part of the chromophore loop (*65*, *67*). The PAS domain functions in proteins regulating the circadian rhythms as a protein dimerization motif and mediates associations between different members of the PAS protein family (*68*, *69*). PYP is believed to be a signal transducer in negative phototaxis, but little is known at present about the mechanism of information transfer. The current results on the solution structure and dynamics of the ground state of PYP provide a basis for further structural studies of the photocycle intermediates, potentially involved in signal transduction.

ACKNOWLEDGMENT

We thank Dr. John Martin and Helena Domingues for helpful discussions. We are also grateful to Dr. Hans Vis for providing the relaxation software and to Nocky Derix for the preparation of figures. Furthermore we thank Mr. H. L. Dekker for the mass spectral analysis and Mr. R. Cordfunke for the isolation and purification of PYP.

SUPPORTING INFORMATION AVAILABLE

A list of chemical shifts for the proton and nitrogen assignments, a list of the dynamic parameters of PYP, which are discussed in the text, a figure with the Ramachandran plot, and a figure with the regression of $J(\omega_N)$ versus $J_{eff}(0)$ for each NH vector of the protein backbone (11 pages). Ordering information is given on any current masthead page.

REFERENCES

1. Meyer, T. E. (1985) *Biochim. Biophys. Acta 806*, 175−183.
2. Meyer, T. E., Yakali, E., Cusanovich, M. A., and Tollin, G. (1987) *Biochemistry 26*, 418−423.
3. Kort, R., Hoff, W. D., Van West, M., Kroon, A. R., Hoffer, S. M., Vlieg, K. H., Crielaard, W., Van Beeumen, J. J., and Hellingwerf, K. J. (1996) *EMBO J. 15*, 3209−3218.
4. Sprenger, W. W., Hoff, W. D., Armitage, J. P., and Hellingwerf, K. J. (1993) *J. Bacteriol. 175*, 3096−3104.
5. Meyer, T. E., Tollin, G., Causgrove, T. P., and Blankenship, R. E. (1991) *Biophys. J. 59*, 988−991.
6. Hoff, W. D., van Stokkum, I. H. M., van Ramesdonk, H. J., van Brederode, M. E., Brouwer, A. M., Fitch, J. C., Meyer, T. E., van Grondelle, R., and Hellingwerf, K. J. (1994) *Biophys. J. 67*, 1691−1705.
7. Kort, R., Vonk, H., Xu, X., Hoff, W. D., Crielaard, W., and Hellingwerf, K. J. (1996) *Biochemistry 35*, 1274−1281.
8. Xie, A., Hoff, W. D., Kroon, A. R., and Hellingwerf, K. J. (1996) *Biochemistry 35*, 14671−14678.
9. Hoff, W. D., Düx, P., Hård, K., Devreese, B., Nugteren-Roodzant, I. M., Crielaard, W., Boelens, R., Kaptein, R., Van Beeumen, J., and Hellingwerf, K. J. (1994) *Biochemistry 33*, 13959−13962.
10. Baca, M., Borgstahl, G. E. O., Boissinot, M., Burke, P. M., Williams, D. R., Slater, K. A., and Getzoff, E. D. (1994) *Biochemistry 33*, 14369−14377.
11. Borgstahl, G. E. O., Williams, D. R., and Getzoff, E. D. (1995) *Biochemistry 34*, 6278−6287.
12. Kim, M., Mathies, R. A., Hoff, W. D., and Hellingwerf, K. J. (1995) *Biochemistry 34*, 12669−12672.
13. Genick, U. K., Borgstahl, G. E. O., Ng, K., Ren, Z., Pradervand, C., Burke, M. P., Srajer, V., Teng, T.-Y., Schildkamp, W., McRee, D. E., Moffat, K., and Getzoff, E. D. (1997) *Science 275*, 1471−1475.
14. Hoff, W. D., Kwa, S. L. S., van Grondelle, R., and Hellingwerf, K. J. (1992) *Photochem. Photobiol. 56*, 529−539.
15. Evans, C. G. T., Herbert, J., and Tempest, D. W. (1970) *Methods Microbiol. 2*, 277−327.
16. Bothner-By, A. A., Stephens, R. L., and Lee, Y. M. (1984) *J. Am. Chem. Soc. 106*, 811−813.
17. Kessler, H., Griesinger, C., Kerssebaum, R., Wagner, K., and Ernst, R. (1987) *J. Am. Chem. Soc. 109*, 607−609.
18. Bodenhausen, G., and Ruben, D. J. (1980) *Chem. Phys. Lett. 69*, 185−189.
19. Marion, D., Driscoll, P. C., Kay, L. E., Wingfield, P. T., Bax, A., Gronenborn, A. M., and Clore, G. M. (1989) *Biochemistry 28*, 6150−6156.
20. Ikura, M., Bax, A., Clore, G. M., and Gronenborn, A. (1990) *J. Am. Chem. Soc. 112*, 9020−9022.
21. Davis, A. L., Keeler, J., Laue, E. D., and Moskau, D. (1992) *J. Magn. Reson. 98*, 207−216.
22. Cavanagh, J., Palmer, A. G., III, Wright, P. E., and Rance, M. (1991) *J. Magn. Reson. 91*, 429−436.
23. Kay, L. E., Keifer, P., and Saarinen, T. (1992) *J. Am. Chem. Soc. 114*, 10663−10665.
24. Vuister, G. W., and Bax, A. (1993) *J. Am. Chem. Soc. 115*, 7772−7777.
25. Düx, P., Whitehead, B., Boelens, R., Kaptein, R., and Vuister, G. W. (1997) *J. Biomol. NMR 10*, 301−306.
26. Whitehead, B., Tessari, M., Düx, P., Boelens, R., Kaptein, R., and Vuister, G. W. (1997) *J. Biomol. NMR 9*, 313−316.
27. Kleywegt, G. J., Vuister, G. W., Padilla, A., Knegtel, R. M. A., Boelens, R., and Kaptein, R. (1993) *J. Magn. Reson., Ser. B 102*, 166−176.
28. Medvedeva, S., Simorre, J. P., Brutscher, B., Guerlesquin, F., and Marion, D. (1993) *FEBS Lett. 333*, 251−256.
29. Dayie, K. T., and Wagner, G. (1994) *J. Magn. Reson., Ser. A 111*, 121−126.
30. Farrow, N. A., Muhandiram, R., Singer, A. U., Pascal, S. M., Kay, C. M., Gish, G., Shoelson, S. E., Pawson, T., Forman-Kay, J. D., and Kay, L. E. (1994) *Biochemistry 33*, 5984−6003.
31. Vis, H., Vorgias, C. E., Wilson, K. S., Kaptein, R., and Boelens, R. (1998) *J. Biomol. NMR* (in press).
32. Peng, J. W., and Wagner, G. (1994) *Methods Enzymol. 239*, 563−596.
33. Delaglio, F., Grzesiek, S., Vuister, G. W., Zhu, G., Pfeifer, J., and Bax, A. (1995) *J. Biomol. NMR 6*, 277−293.
34. Press, W. H., Teukolsky, S. A., Vettering, W. T., and Flannery, B. P. (1992) *Numerical Recipes*, Cambridge University Press, Cambridge, U.K.
35. Nilges, M. (1995) *J. Mol. Biol. 245*, 645−660.
36. Nilges, M., Clore, G. M., and Gronenborn, A. M. (1988) *FEBS Lett. 229*, 317−324.
37. Brünger, A. T. (1992) *X-PLOR. A system for X-ray crystallography and NMR*, Yale University Press, New Haven, CT.
38. Laskowski, R. A., Rullmann, J. A. C., MacArthur, M. W., Kaptein, R., and Thornton, J. M. (1996) *J. Biomol. NMR 8*, 477−486.
39. Hutchinson, E. G., and Thornton, J. M. (1996) *Protein Sci. 5*, 212−220.
40. Koradi, R., Billeter, M., and Wüthrich, K. (1996) *J. Mol. Graphics 14*, 51−55.
41. Wüthrich, K. (1986) *NMR of Proteins and Nucleic Acids*, Wiley, New York.
42. Piantini, U., Sørensen, O. W., and Ernst, R. R. (1982) *J. Am. Chem. Soc. 104*, 6800−6801.
43. Shaka, A. J., and Freeman, R. (1983) *J. Magn. Reson. 51*, 169−173.
44. Griesinger, C., Otting, G., Wüthrich, K., and Ernst, R. R. (1988) *J. Am. Chem. Soc. 110*, 7870−7872.
45. Jeener, J., Meier, B. H., Bachman, P., and Ernst, R. R. (1982) *J. Chem. Phys. 71*, 4546−4553.
46. Oschkinat, H., Griesinger, C., Kraulis, P. J., Sørensen, O. W., Ernst, R. R., Gronenborn, A. M., and Clore, G. M. (1988) *Nature 332*, 374−376.

47. Vuister, G. W., Boelens, R., and Kaptein, R. (1988) *J. Magn. Reson. 80*, 176−185.
48. Neri, D., Szyperski, T., Otting, G., Senn, H., and Wüthrich, K. (1989) *Biochemistry 28*, 7510−7516.
49. Brooks, B., Bruccoleri, R., Olafson, B., States, D., Swaminathan, S., and Karplus, M. (1983) *J. Comput. Chem. 4*, 187−217.
50. Kabsch, W., and Sander, C. (1983) *Biopolymers 22*, 2577−2637.
51. Peng, J. W., and Wagner, G. (1992) *J. Magn. Reson. 98*, 308−332.
52. Lefèvre, J.-F., Dayies, K. T., Peng, J. W., and Wagner, G. (1996) *Biochemistry 35*, 2674−2686.
53. Brüschweiler, R., Liao, X., and Wright, P. E. (1995) *Science 268*, 886−889.
54. Lee, L. K., Rance, M., Chazin, W. J., and Palmer, A. G., III (1997) *J. Biomol. NMR 9*, 287−298.
55. Lipari, G., and Szabo, A. (1982) *J. Am. Chem. Soc. 104*, 4546−4559.
56. Lipari, G., and Szabo, A. (1982) *J. Am. Chem. Soc. 104*, 4559−4570.
57. Clore, G. M., Driscoll, P. C., Wingfield, P. T., and Gronenborn, A. M. (1990) *Biochemistry 29*, 7387−7401.
58. Wagner, G. (1993) *Curr. Opin. Struct. Biol. 3*, 748−754.
59. Yu, V. Y., Pervushin, K. V., Korzhnev, D. M., and Arseniev, A. S. (1995) *J. Biomol. NMR 6*, 113−122.
60. Bax, A., and Tjandra, N. (1997) *Nat. Struct. Biol. 4*, 254−256.
61. Vriend, G. (1990) *J. Mol. Graphics 8*, 52−56.
62. Morris, A. L., McArthur, M. W., Hutchinson, E. G., and Thornton, J. M. (1992) *Proteins 12*, 345−364.
63. Scrutton, N. S., and Raine, R. C. (1996) *Biochem. J. 319*, 1−8.
64. Genick, U. K., Devanathan, S., Meyer, T. E., Canestrelli, I. L., Williams, E., Cusanovich, M. A., Tollin, G., and Getzoff, E. D. (1997) *Biochemistry 36*, 8−14.
65. Crosthwaite, S. K., Dunlap, J. C., and Loros, J. J. (1997) *Science 276*, 763−769.
66. Nambu, J. R., Lewis, J. O., Wharton, K. A., Jr., and Crews, S. T. (1991) *Cell 67*, 1157−1167.
67. Lagarias, D. M., Wu, S.-H., and Lagarias, J. C. (1995) *Plant Mol. Biol. 29*, 1127−1142.
68. Huang, J. Z., Edery, I., and Rosbash, M. (1993) *Nature 364*, 259−262.
69. Lindebro, M. C., Poellinger, L., and Whitelaw, M. L. (1995) *EMBO J. 14*, 3528−3539.

BI9806652